Int. J. Microgravity Sci. Appl. 32 (2) 2015, 320207
DOI :10.15011/ijmsa.32.320207

IIIII The Kikuchi-Kossel Experiment - Colloidal Crystals under Microgravity IIIII
(Original Paper)

Gas-Liquid-Solid Condensation of Gravitationally Confined Polystyrene Particles near a Charged Wall at Intermediate Screening Lengths

Masamichi ISHIKAWA [1], Shun ITO [2], Saki MIYOSHI [3] and Junko HABASAKI [4]

Abstract

Charged polystyrene particles, which were initially sedimented uniformly on a glass wall, spontaneously transformed into two-dimensional gas, liquid, and solid phases in aqueous solvents. Their relative stabilities could be determined by a common phase diagram consisting of gas-liquid and liquid-solid coexistence lines under the conditions of a large particle radius ($a >> \kappa^{-1}$) and intermediate screening length (a=1.5 μm and 10 nm<κ^{-1}<300 nm), where a is the particle radius and κ is the Debye-Hückel parameter. The gas-liquid miscibility gap which had a critical point was very stable over a wide range of salt concentrations. The radial distribution functions of colloidal particles in the liquid phase showed remarkable oscillatory damping and both short-range (~particle diameter σ) and long-range (>10σ) decay lengths were found. The latter was attributed to the charge density wave (CDW) due to alternating layers of oppositely charged colloids and counterions along the radial coordinate. Because the charged glass wall had a similar surface charge density and sign as the particles, the repulsive levitation at the wall against gravity assisted the thermal rearrangement during phase separation. Further evaluation is promising for investigating the complicated physics of particle-wall interactions.

Keyword(s): Polystyrene, Charged colloid, Colloidal phase transition, Sedimentation.
Received 12 Jan. 2015, accepted 31 Mar. 2015, published 31 Apr. 2015

1. Introduction

Colloidal suspensions have been extensively studied as simple systems for fundamental models of electrical phenomena involving clustering, aggregation, phase separation, and self-organization of charged substances in physics, chemistry, and biology [1-3]. Recently, a colloidal analogue in the Restricted Primitive Model (RPM), which is a symmetrical electrolyte of charged hard sphere anions and cations with equal sizes and charge numbers, has been reported to show similar gas-liquid and liquid-solid phase transitions as RPM simulation results [4-9]. Advances in the understanding of the RPM from both simulations and experiments have stimulated studies on asymmetric electrolytes, called the Primitive Model (PM). Although phase diagrams of the moderately asymmetrical PM have exhibited a similar phase diagram as the RPM, the phase diagram of an extremely asymmetrical electrolyte such as a colloidal suspension in a low ionic strength solution remains unknown due to theoretical and computational difficulties arising from the large size and charge differences [10-12].

Hachisu and co-workers were the first to study the experimental phase diagram of monodispersed polystyrene colloids [13-15]. They showed that polystyrene particles in high ionic strength solutions exhibit an order-disorder phase transition due to hard sphere repulsion (a Kirkwood-Alder transition). Later evidence has suggested that the Kirkwood-Alder transition is not applicable in low ionic strength solutions; the interparticle spacing of polystyrene colloids is shorter than the one estimated from the Kirkwood-Alder transition [16], gas-liquid phase condensation is found in charged colloidal suspensions [17], and void structures of pure solvents surrounded by dense latex phases are formed under neutral buoyancy conditions using a D_2O-H_2O mixture [18, 19]. To explain these findings, Sogami and Ise proposed a modified pair potential where like-charged colloids introduce an attractive term into the common DLVO potential [20]. Debates on the validity of the attractive term have triggered intense theoretical and experimental activities, which are reviewed in Refs. 2), 16) and 21). Hence, an experimental phase diagram that tests the predicted gas-liquid-solid phase behavior is urgently needed to resolve mutually contradictory arguments such as whether like-charged colloids possess an attractive or repulsive interaction in deionized water.

The two-dimensional confinement of colloidal suspensions

1 RIKEN, Research Cluster for Innovation, 2-1 Hirosawa, Wako, Saitama 351-0198, Japan.
2 Sysmex Corp. Ltd., 1-5-1, Wakinohama-kaigandori, Chuo-ku, Kobe, Hyogo 651-0073, Japan.
3 MRI Research Associates, Inc., 1-13-1 Uchi-Kanda, Chiyoda-ku, Tokyo 101-0047, Japan.
4 Tokyo Institute of Technology, 4259 Nagatsuta, Midori-ku, Yokohama, Kanagawa 226-8502, Japan.
(E-mail: masamichi.ishikawa@riken.jp)

coupled with digital-microscopic measurements has been widely recognized as a useful experimental configuration to study the physical characteristics of colloidal interactions. Grier and his coworkers have reported an attractive pair potential between like-charged colloids confined between two parallel plates whose separation is slightly larger than the particle diameter or less than 200 μm if the particles are sedimented on the bottom plate [22]. Because the attractive potential disappeared when the bottom plate was coated by Au but the other parameters remained unchanged, the attraction is considered to have a purely electrostatic origin. However, it should be noted that optical artifacts caused a systematic error in the interparticle distance measurements due to the overlap of neighboring particle's light spots. Consequently attractive potentials were falsely obtained via data processing [23]. Lobaskin et al. have investigated the inverse problem to extract effective pair potentials from an experimentally measured two-dimensional radial distribution function at high colloidal densities and under low salt conditions [24-26]. They found that for polystyrene particles with 2.4 and 3 μm diameters, the effective pair potentials had a long-range attractive part, which depended on the colloidal densities at $\rho\sigma^2$=0.23, where ρ is the particle number density in two-dimensions and σ is the particle diameter[26]. These results suggest the possibility of colloidal phase separation on the substrate at high particle densities and surface charges. However, the debate continues [27] as complex physics involving charged colloids near interfaces (e.g. image-charge effects due to dielectric discontinuity, surface charge of a wall, or hydrodynamic interactions) requires further consideration.

This study aims to investigate the phase behaviors of two-dimensional colloidal dispersions at higher particle densities than those previously reported. Herein we employ gravitationally confined colloidal dispersions near a charged wall. The charged colloids are denser than the solvent and they have sufficient particle sizes to suppress the diffusional flotation of the particles from the substrate, therefore the colloids can form a mono-particle layer under sedimentation equilibrium. The two-dimensional configuration of particle system facilitates the quantitative characterization of phase behaviors using the coordinates of particles directly obtained by the image of optical microscope. We construct gas-liquid and liquid-solid phase diagrams according to the structural characterization by density, coordination number and radial distribution function and a universal mechanism of the observed phase behaviors is considered.

2. Experimental Techniques

2.1 Colloid, cell, and sample preparation

The colloidal particles of sulfonated polystyrene (PS) microspheres (0.993±0.021 μm and 3.004±0.029 μm in diameter) were obtained from Duke Sci. Corp. The colloidal particles were dispersed in an aqueous solution. Prior to use, the suspension was deionized using ion exchange resins to remove the small amount of unknown dispersants and preservatives in the aqueous suspension. We placed a mixed-bed ion exchange resin, Bio-RAD-501-X8(D), in the suspensions, and they were kept in contact for 1 to 5 months in a glass vessel. The treatment worked well as the phase separation was reproducible. The experimental cell was composed of crown glass with a disk-shaped inner volume that had a 10.0 mm diameter and 0.5 mm thickness (**Fig. 1**).

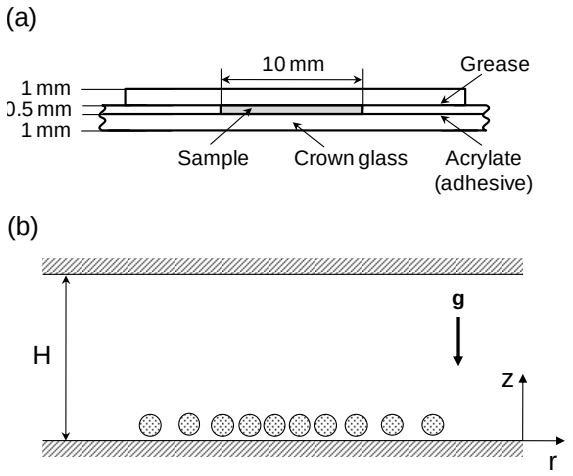

Fig. 1 Schematic view of the optical cell for colloidal condensation. (a) Optical cell composed of crown glass. Lower and middle glasses are bonded by acrylate, and the upper glass is sealed using vacuum grease. (b) Adjusting the solvent density by mixing 50% of ethanol (EtOH) with water enhances the gravitational sedimentation of polystyrene latex. Mono-particle layer is maintained during condensation. Coordinates are defined by z (vertical direction) and r (radial direction). Height H is 500 μm.

The lower and middle glass plates were bonded by acrylate (DYMAX OP-4-20632-H). The horizontal roughness of the glass surface, which was in contact with the colloidal suspension, was evaluated using an optical surface profiler, ZYGO's NewView. The obtained average vertical difference was 162 nm (±81 nm). Since a particle of the average kinetic energy of 0.5kT per a degree of freedom can overcome the difference, such a surface roughness is neglected in the discussion. To prevent carbon dioxide contamination from the air, the glass cover was carefully sealed using vacuum grease, and air bubbles were excluded when the samples were filled. The packing fraction of each phase remained constant for 80 hours, confirming careful sample preparation. The cell was located on a flat, horizontal metal plate to diminish the temperature gradient and the inclination to gravity. The particle

concentration was varied from 0.001 to 0.20 vol %. KCl was added as a salt with a concentration ranging from 0−1 mM. The experiments were conducted at room temperature (20±2 °C).

Mixing water with ethanol with a volume ratio ranging from 0 to 50% of ethanol enhanced the sedimentation force of the particles, and realized mono-particle layer condensation on the bottom plate. Prior to use, both solvents were fully deionized by the ion exchange resin. The density of the solvent was determined so that nearly 100% of the particles were distributed within the thickness of their diameter, assuming the sedimentation equilibrium density profile $n(z)$ [28, 29].

$$n(z) = n_0 \exp\left(-\frac{zPe}{H}\right) \tag{1}$$

where z is the height from the bottom of the cell, n_0 is the particle number at $z = 0$, and H is the height of the cell., where $Pe = HU_0 / D_0$, Pe is the Peclet number, U_0 is the stationary-state sedimentation velocity (the Stokes velocity) determined by the balance between the gravitational force and the viscous drag, and D_0 is the diffusion coefficient calculated from Stokes-Einstein law [29]. Equation (1) is valid for realistic colloids approaching infinite dilution. The mono-particle layer sedimentation was confirmed using confocal laser scanning microscopy, CLSM (OLYMPUS Corp., Japan). An inverted optical microscope (IX71, OLYMPUS Corp.) with objective lenses of 20× and 60× was used for *in situ* observations of the colloidal condensation at the bottom of the cell.

2.2 Zeta potentials of colloids

Colloid stability was tested by measuring the time dependency of their zeta potentials after placing an ion-exchange resin into stock suspensions (0.43 vol %). The zeta potentials of the colloids in various salt concentrations were determined by the laser-Doppler method using analytical equation 4.20 in the paper of O'Brien and Hunter [30-34]. When the measured sample was in the range of intermediate κa, this equation had a maximum mobility above 40 mV with the absolute value of the zeta potential; two zeta potentials (low and high values) were found. A detailed discussion to determine the true value from these two possibilities is reported elsewhere [33), 36-39]. Although deionization of the colloidal samples was necessary to reproduce the phase separation experiments, it reduced the stability against particle coagulation during storage (1 to 5 months in this work). **Table 1** shows the results of zeta potential measurements at 2.5 and 5 months after treatment. Additionally, the table compares the zeta potentials of the particles at various added salt concentrations (1 to 1000 μM). Both the 2.5 and 5 month samples in a batch had nearly the same value, and an abnormal potential was not detected. The colloids treated during this period were used in the following experiments.

Table 1 Zeta (ζ) potential measurements of colloids at 2.5 and 5 months after treatment under the added salt conditions. Solvent is water at room temperature.

Salt (M)	κa	ζ potential (mV)	
		2.5 months	5 months
1.0E-06	4.9	-40	-55
1.0E-05	15.7	-53	-63
1.0E-04	49	-77	-89
1.0E-03	157	-95	-97

2.3 Microscopic image analysis

The phase behaviors of the colloids were observed using an inverted microscope with a thermoelectrically cooled CCD camera (DP72, Olympus Corp.). About 1000−1300 particles were captured per frame, and their numerical positions were determined using image analysis software ImageJ [35]. The precision of the coordinate measurements was ±0.07 μm. To compare the quasi-two-dimensional phase diagram with previously reported ones, the packing fraction $\eta = (4/3)\pi a^3 N / 2aS$ was adopted instead of the two-dimensional reduced density , where N is the number of particles inside the measured bottom area S. The two-dimensional radial distribution function *g*(r) was analyzed using Eq. (2).

$$g(r) = \frac{S}{N(N-1)} \sum_{k=1}^{N-1} \frac{n_k\left(r - \Delta r/2, r + \Delta r/2\right)}{2\pi r \Delta r} \tag{2}$$

Where $n_k(r - \Delta r/2, r + \Delta r/2)$ is the number of particles found in a shell with radius *r* and thickness Δr with the shell centered on the *k*-th particle. The running coordination number *CN*(r) of a particle in a phase is defined as

$$CN(r) = \frac{N-1}{S} \int_0^r 2\pi r' g(r') dr' \tag{3}$$

The coordination number (*CN*) was calculated using Eq. (3) at the radial position where the radial distribution function had the first minimum. Because the cutoff length of *g*(r) was set to 20 μm, particles 20 μm inside the rectangular boundaries were evaluated as center particles in the *g*(r) and *CN*(r) calculations.

3. Results

3.1 Gravitational confinement of colloids near charged wall

The density profile of gravitational sedimentation for polystyrene particles (3 μm) was measured by changing the solvent density, according to Eq. (1). The *Pe* number was controlled by ethanol content in the range of 0 to 50 vol %. **Figure 2** shows the natural logarithm of $n(z)/n_0$ as a function of z at the initial particle concentration of 0.2 vol %. The concentration was set at 50% area occupation of particles under

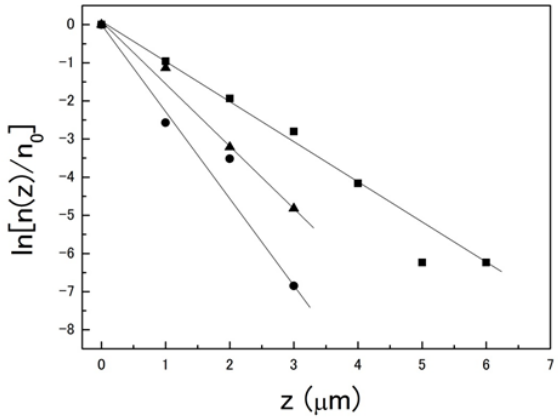

Fig 2 Sedimentation profile of polystyrene particles in EtOH/water mixed solvents. The solvent density was controlled by mixing ethanol of 0% (■), 12.5% (▲) and 25% (●) without added salt. The profiles were measured after 48 hours of sample preparation at room temperature.

the condition of monolayer sedimentation on the substrate. As shown in **Fig. 2**, the density profile decreased exponentially and the calculated *Pe* for each ethanol content of 0, 12.5 and 25% was 320, 770 and 980, respectively. No particle separating from the substrate was observed in the case of 50% ethanol content. The condition of mono-particle layer sedimentation is estimated at more than *Pe*=1500 for polystyrene particles.

The sedimentation rate at the bottom position was measured in 50% EtOH/water solvent. **Figure 3(a)** shows the results with respect to different salt concentrations (0–1 mM), and demonstrates that the sedimentation equilibrium at the bottom was reached after 50 minutes. There was no second-layer particle at this moment. The particle number of the no added salt case was systematically higher than the case of added salt during the sedimentation period, indicating the possibility of particle-particle interaction. The lateral concentration of colloids after equilibrium sedimentation was prominent as described in the next paragraph. Although the interaction among colloids was not excluded during the sedimentation, the sedimentation profiles in **Fig. 3(a)** and the mono-layer particle sedimentation are approximately predicted by Eq. (1). Additionally, the optical microscopy observation showed an active thermal agitation of the particles on the substrate. It should be noted that the sedimented particles levitated on the surface against gravity.

Unlike in the sedimentation process, an anomalous condensation of the particles proceeded very slowly. After sedimentation, the colloidal suspension was gradually pulled toward the center of the cell, as shown in **Fig. 3(b)**, and its periphery left a paddle-like shape (1–4 h after sample preparation). The interface of the condensate exhibited a

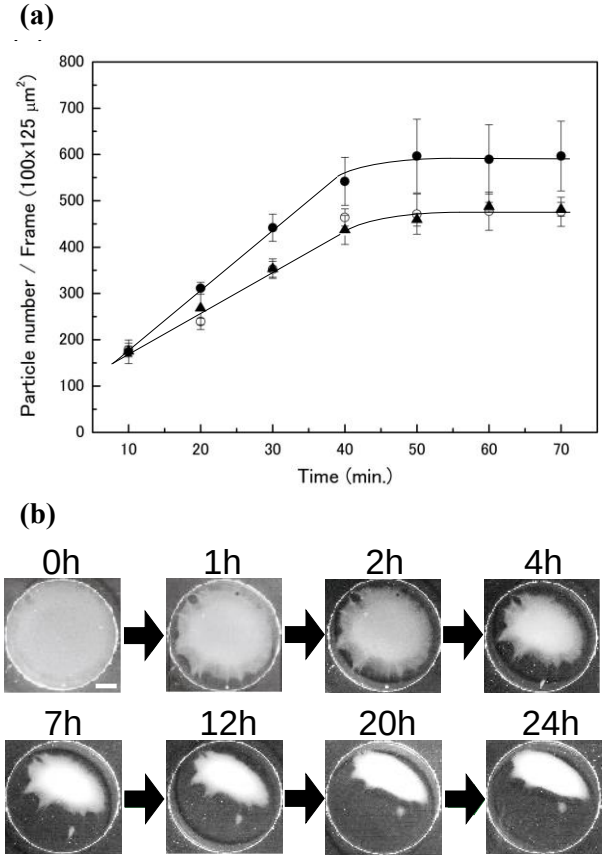

Fig. 3 Sedimentation of polystyrene particles and colloidal condensation after sedimentation. (a) Increase in the particle number per CLSM frame on the bottom plate as a function of time. ●: No added salt, ○: 10^{-5}M KCl, ▲: 10^{-3}M KCl. Error bars were estimated using the data from the different fields of view within the same sample. (b) Time series of macroscopic photographs of colloidal condensation after sample preparation using polystyrene particles with a 3 μm diameter. Colloidal particles are initially suspended in water (0.05 vol %, 10^{-5}M KCl) at room temperature. The scale of the white bar in the photographs of 0 h is 2 mm and the same scale are used through the photographs.

boundary, and the surface area occupied by the condensate maintained a constant value beyond 20 hours. Gradually altering the image brightness inside the condensate revealed an internal density stratification, especially at the center for high-density condensation of the colloids. The macroscopic density profile for colloidal condensation is discussed in the next section.

A similar sedimentation experiment using the PS colloids with a 1 μm diameter and 50 vol % EtOH/water solvent was executed. As expected from Eq. (1), many particles were distributed along the vertical axis from the bottom surface at equilibrium sedimentation. Similarly, the colloids condensed and the projected area of the condensate to the bottom reached a constant value over time. **Figure 4** shows the area reduction in

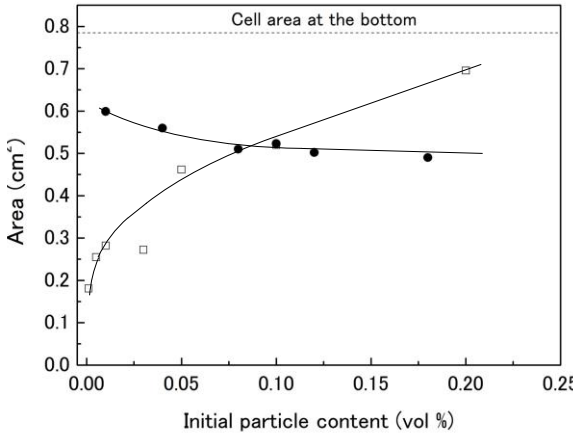

Fig. 4 Area reduction in equilibrium colloidal condensation as a function of initial particle content. Without added salt and 50 vol % EtOH/water solvent at room temperature (25 °C). Symbols ● and □ denote the results of the PS particles with diameters of 3 μm and 1 μm, respectively.

equilibrium condensation for 1 μm and 3 μm particles as a function of the initial particle content. Both colloids showed the condensation even with the initial dilute particle content (0.001 and 0.01 vol % for 1 μm and 3 μm, respectively).

However, one remarkable difference was observed; the particle content area decreased for 3 μm, whereas that for 1 μm increased. These differences are attributed to the mono-layer and multi-layer particle condensations. Mono-layer condensation has a restricted area due to two-dimensionally closest packing, but this type of restriction does not exist in the other case due to the three-dimensional expansion in the free volume. For either case, the area depended on the initial particle content. That is, the interacting mechanism to strengthen the condensation depended on the particle density. These results strongly indicate that PS colloids with a 3 μm diameter are gravitationally confined near the bottom wall when they are dispersed in 50 vol % EtOH/water solvent.

3.2 Colloidal gas-liquid-solid condensation

To realize two-dimensional (mono-layer) condensation, the initial particle content was limited to 0.1–0.2 vol %, which corresponds to a bottom area occupation of 25–50% after complete sedimentation. As explained above, the colloidal suspension was pulled toward the center of the cell after sedimentation. Additionally, the higher density region appeared in the center of the condensate, while the lower density region was located near the periphery. A microscopic determination of the suspension densities indicated four relatively homogeneous regions along the radial direction, which are denoted as A, B, C and D in **Fig. 5(a)**. Time dependency measurements of each

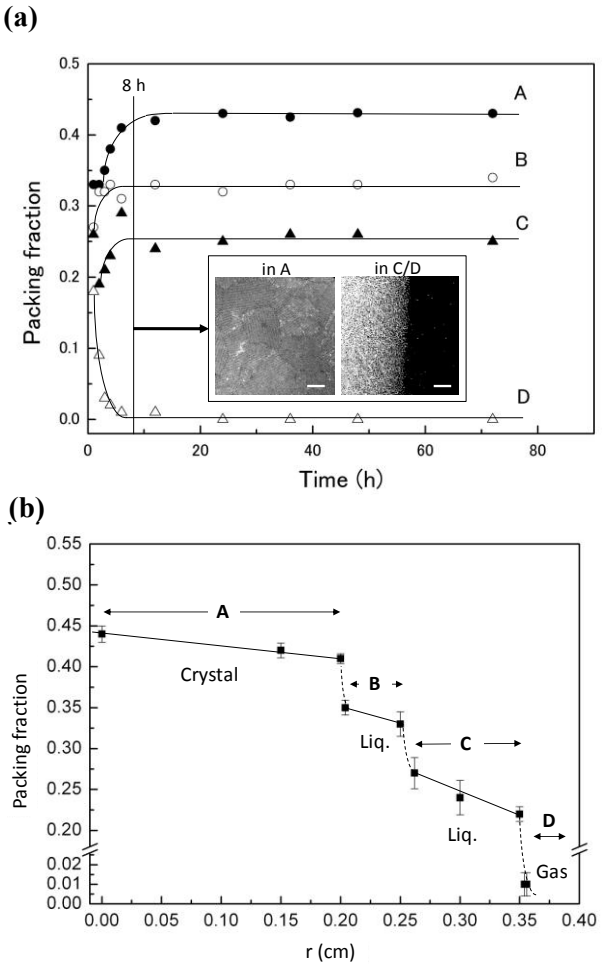

Fig. 5 Macroscopic density distribution in colloidal condensation. Initial particle content is 0.2 vol % in 50% EtOH/water solvent containing 10^{-6} M KCl. (a) Packing fractions inside the suspension as a function of time. Symbols, A (●), B (○), C (▲) and D (△) indicate the fractions in the decreasing order. Inset shows the microscopic images of the crystalline region (A) and liquid/gas interfacial region (C/D) after 8 hours. Bars indicate 100 μm lengths. (b) Equilibrium distribution of the packing fraction observed after 48 hours as a function of distance *r* from the center of the condensate.

density confirmed that about 40 hours were sufficient to reach the equilibrium density distribution. The inset of **Fig. 5(a)** shows microscopic photographs after 8 hours in region A and the interfacial region (C/D), which represent the crystalline and liquid/gas phases, respectively. The crystalline region displayed crystal coalescence originating from nucleation and growth processes, while the particle concentration rapidly decreased in front of the liquid interface.

Each uniform region in **Fig. 5(b)** was structurally characterized by radial distribution functions. The results indicated that regions A, B, C and D corresponded to the crystal, liquid (high-density), liquid (low-density), and gas phase, respectively. According to the preliminary investigation,

Table 2 Experimental conditions and resultant phase separations. Packing fractions are determined in the equilibrated phases after more than 40 hours. Polystyrene particles with 3 μm diameters and deionized water containing 50 vol % ethanol are used. KCl is added as a salt, and the temperature is 20±2 °C during the experiments.

No.	Phase	PS vol %	Salt M	Packing fraction η
1	Gas	0.1	1.00E-06	0.008±0.004
2		0.2	5.00E-06	0.010±0.004
3		0.2	1.00E-05	0.007±0.004
4		0.2	1.00E-04	0.021±0.008
5	Liquid (low-density)	0.1	8.20E-07	0.285±0.015
6		0.2	1.00E-06	0.28±0.01
7		0.2	5.00E-06	0.24±0.021
8		0.2	1.00E-05	0.258±0.026
9		0.2	5.00E-05	0.254±0.001
10		0.2	1.00E-04	0.231±0.017
11		0.1	2.50E-04	0.20 [a]
12		0.1	5.00E-04	0.19 [a]
13		0.1	1.00E-03	0.16 [a]
14	Liquid (high-density)	0.2	1.00E-06	0.34±0.018
15		0.2	5.00E-06	0.34±0.011
16		0.2	1.00E-05	0.339±0.016
17		0.2	2.00E-05	0.325±0.018
18		0.2	1.00E-04	0.340±0.032
19	Solid (hexagonal crystal)	0.2	8.20E-07	0.38±0.008
20		0.2	8.70E-07	0.38±0.009
21		0.2	1.00E-06	0.40±0.01
22		0.2	2.00E-06	0.393±0.004
23		0.2	5.00E-06	0.402±0.002
24		0.2	5.00E-06	0.44±0.013
25		0.2	8.00E-06	0.397±0.007
26		0.2	1.00E-05	0.395±0.005
27		0.2	1.00E-05	0.401±0.018

[a] Errors were not determined due to large density fluctuations.

we systematically constructed gas-liquid and liquid-solid phase diagrams with respect to the packing fraction and salt concentration. Note that the phases appeared simultaneously in a condensation experiment. **Table 2** summarizes the experimental conditions and the resultant packing fractions of the corresponding phases. The 18 samples were evaluated to obtain the data in **Table 2** and the error bars of the packing fraction were estimated from the 4 different fields of view within the same sample.

3.3 Construction of phase diagrams

To compare the phase diagrams with the reported diagrams, which were obtained by theories, MC simulations etc., a relationship between the reduced temperature and the salt concentration at the colloidal limit is applied. The relationship is defined as a highly asymmetrical system of like-charged colloidal particles and monovalent (point) counterions in the presence of a low concentration of added salt. Because colloid ions are negatively charged in normal solvents, their charge can be defined as $-Z_{-}e$, where e is the unit charge and Z_{-} is the absolute value of the charge. Similarly, the counterions have a charge of $Z_{+}e$. The sizes of the colloid ions and counterions are σ_{-} ($=2a$) and σ_{+}, respectively. Highly charged colloidal particles and point-like counterions with a unit charge enable the limit to be set at $\sigma_{+} \to 0$ and $Z_{+}=1$.

At this colloidal limit, the reduced temperature T^{*} is defined as [6, 7]

$$T^{*} = \frac{(1+\kappa\sigma_{+}/2)(1+\kappa\sigma_{-}/2)\sigma_{+-}}{Z_{+}Z_{-}l_{B}} \approx \frac{(1+\kappa a)a}{Z_{-}l_{B}} \qquad (4)$$

Where $\sigma_{+-}=(\sigma_{+}+\sigma_{-})/2$. In 50% ethanol/water solvent, the Bjerrum length is calculated as 1.09 nm at 25 °C (*Handbook of Chemistry and Physics*, CRC Press, 2003). The Debye parameter κ is $\kappa=\sqrt{8\pi l_{B}c}$ when a 1:1 electrolyte such as KCl with concentration c is used. Thus, T^{*} can be rescaled by the salt concentration of the colloidal suspension at a constant temperature. However, the effective surface charge of colloids increased from 2.0×10^{4} to 1.2×10^{6} according to the increase in the salt concentration from 1 μM to 1 mM, and showed a saturated aspect [33]. Because the saturated surface charge originated from the nonlinear condensation of the counterions in the vicinity of the colloid ions, the rescaling of temperature by concentration should be carefully interpreted at high salt concentrations because it happens to underestimate the temperature due to the very large effective charge. According to this reason, the salt concentration is kept in the following phase diagrams as an alternative of temperature.

Figure 6 shows the gas-liquid phase diagram constructed by measuring the packing fraction of the phases at each KCl concentration, where the packing fraction (η) is the abscissa and the salt concentration is the ordinate. The phase boundaries were identified according to the coordination number (CN) and radial distribution function of each phase.

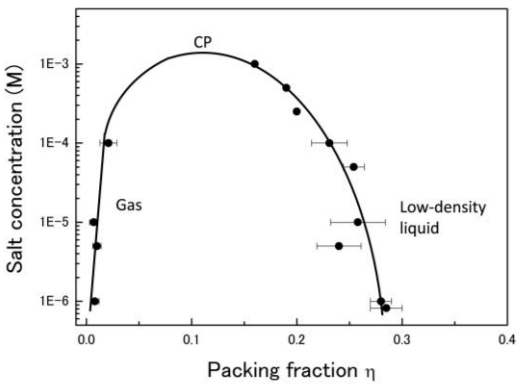

Fig. 6 Colloidal gas-liquid phase diagram. **Table 2** lists the data used. Solid curve denotes the gas-liquid coexistence with a critical point (CP). Revised phase diagram of the previously reported one [33] is shown, where the newly obtained data are plotted with error bars and both the gas and liquid coexistence lines are given.

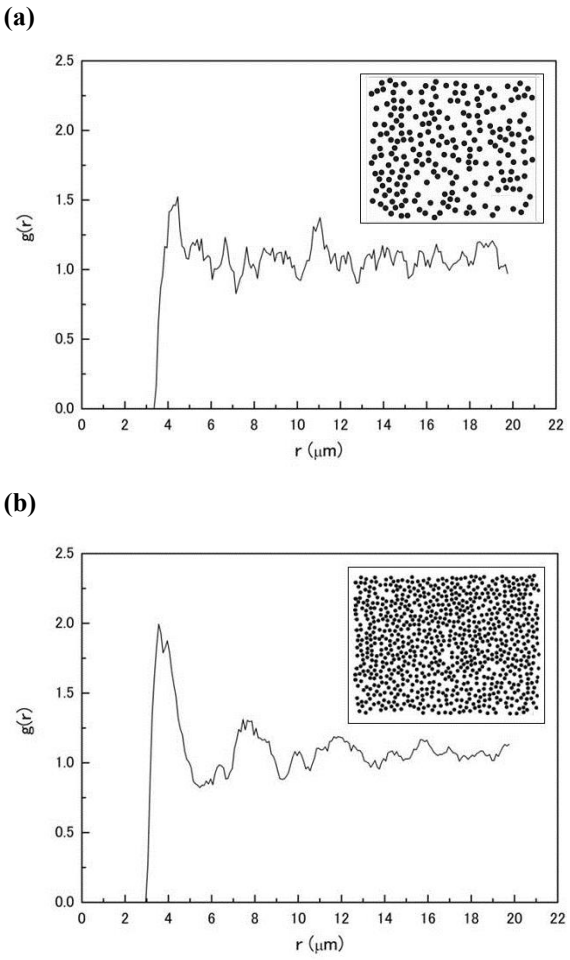

Fig. 7 Radial distribution functions g(r) of the gas and liquid phases. (a) Gas phase. Initial particle content is 0.1 vol % in 50% ethanol/water containing 10^{-6} M KCl. (b) Liquid phase (low density). Initial particle concentration is 0.2 vol % in the 50% ethanol/water containing 10^{-5} M KCl. Inset shows the particle configuration of each phase.

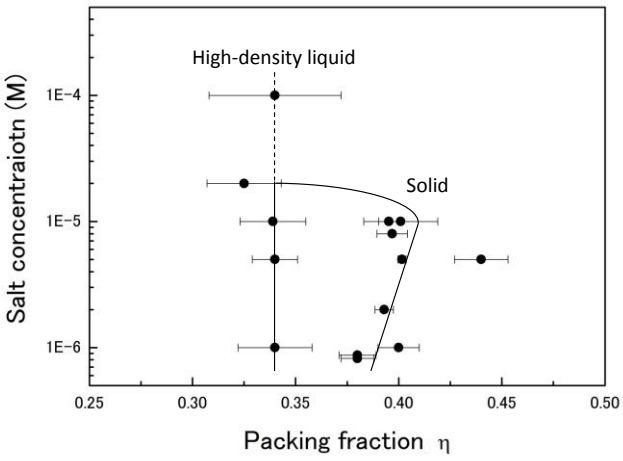

Fig. 8 Colloidal liquid-solid phase diagram. **Table 2** lists the data. Solid curve shows the liquid-solid coexistence, and the dashed line indicates an extension of the liquid-line beyond the solid-line.

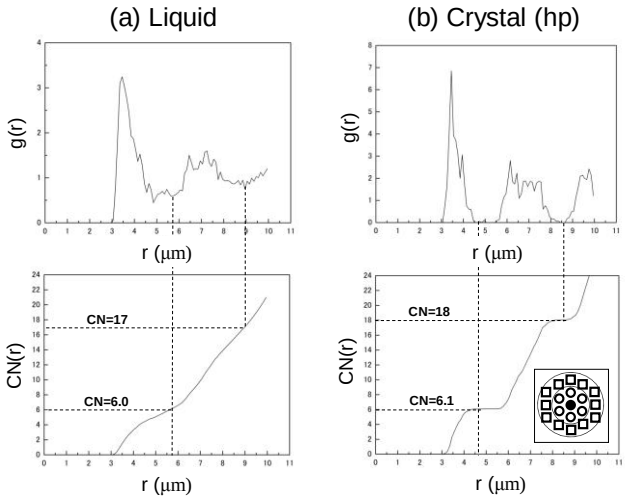

Fig. 9 Radial distribution functions and running coordination numbers of high-density liquid and hexagonally packed (hp) crystals. (a) and (b) show the first and second coordination numbers, which correspond to the first and second minima of the radial distribution function of each phase, respectively. 0.2 vol % polystyrene particles (diameter 3 μm) are suspended in 50 vol % water/ethanol mixed solvent containing 10^{-5} M KCl.

As previously reported [33], the gas-liquid miscibility gap reached a critical point (CP) and showed a critical density fluctuation near the CP. The CP appeared at a packing fraction of 0.11 and a salt concentration of 1 mM. To characterize the structural aspects of the observed phases, the radial distribution function g(r) was calculated using the position of the particles from each microscopic image. **Figure 7** shows the radial distribution functions of the gas and liquid phases with snapshots of the particle configurations, and gives coordination numbers of <1.0 and ~4.0, respectively.

Figure 8 shows the liquid-solid phase diagram, which has a density gap between the liquid and solid phases below 10 μM KCl. The packing fraction of the solid slightly increased as the salt concentration increased. Hexagonally-packed (hp) crystals were stable under the liquid-solid coexistence, but disappeared above 20 μM. Square-packed crystals were only observed during the initial stage (after 10 hours) of phase separation at the lowest salt concentration, but were ultimately converted into hp crystals. **Figure 9** shows the first and second coordination numbers, which correspond to the first and second minima of the radial distribution function at [KCl]=10 μM. Both the liquid and solid phases had similar coordination numbers (6.0 and 6.1, respectively). These coordination numbers suggest that local clusters with hexagonal coordination are stable in the liquid-solid coexistence.

4. Discussion

4.1 Phase behavior of charged colloids

A colloidal suspension consisting of large colloids and microions (counterions and salt ions) in a homogeneous solvent is physically defined as the limiting case of the PM where the microions are considered to be point-like but have individual electrostatic interactions with other ions as described by Eq. (4). The PM is a multicomponent model different from the DLVO system where one component colloid ions interacts each other and the other small ions are assumed to be screening ions of the electric fields from colloids. Recently, the full phase diagrams of charged colloidal particles using MC calculations are reported and the change of phase stabilities in conjunction with the critical point are discussed as a function of charge asymmetry and salt concentration[10-12]. The obtained phase diagrams are characterized by comparing with the PM phase diagrams.

Hynninen and Panagiotopoulos studied the full phase diagrams of a charge- and size-asymmetric system with colloid charge Q=10 and counterions of charge -1 in the presence of monovalent added salt [12]. The phase diagrams of the gas-liquid-solid phases of the PM (**Fig. 10** of Ref. 12) and this work (**Fig. 6**) indicate a qualitative resemblance; 1) both the phase diagrams consist of familiar gas-liquid and liquid-solid phase coexistence regions, 2) the gas-liquid miscibility gap in the MC calculation appears between 0-0.3 packing fraction and the critical point appears with increasing salt concentration at η^*~0.18 which is similar to the experimental value 0.11, and 3) added salt stabilizes the liquid phase and shrinks liquid-solid coexistence region. Despite the observation, the ability to form the gas-liquid miscibility gap obtained in the experiments differs remarkably from that in the simulations. The MC simulations of the colloidal PM show that the gas-liquid coexists within a rather narrow region at low concentrations; that is, the gas-liquid CP is less stable with respect to liquid-solid coexistence. Contrary to the case of the colloidal PM, the CP in the experiments was stable with respect to the liquid-solid transition. The inverted stability of the liquid-solid transition is attributed to the enhanced electrostatic repulsion between neighboring colloids in the lattice due to the large effective charges as the salt concentration increases.

Another difference appeared in the power-law relationship of reduced critical temperature T_c^* with colloid charge. The relation for the colloidal PM as a function of colloid charge Q is expressed as $T_c^* = 0.27Q^{0.48}$, whereas T_c^* in our results shows a low T_c^* (~0.17) despite the high asymmetry in charge (Q>10^4) [10]. These apparent differences are related to the modified temperature scale due to the increase in the effective charge with salt concentration. Both the effective charge and salt concentration in this work are 10 to 100 times larger than those of the cited references. The conditions of high charge and salt concentration enhance counterion condensation on the colloidal particles. According to Eq. (4), the increase in the reduced temperature with salt concentration in the Debye parameter is cancelled by the simultaneous increase of the colloidal charge in the denominator. Thus, the broad stability region in the packing fraction–salt concentration plane (**Fig. 6**) is greatly reduced in the packing fraction–temperature plane. This causes the aforementioned power-law relationship to become insensitive to the colloidal charge by the apparent decrease of temperature. These discussions indicate that the experimental phase diagrams do not contradict the phase behaviors of the results of the simulations in Ref. 10.

4.2 Universal aspects of the interaction between charged colloids

Analysis of the radial distribution function $g(r)$ provides useful information to specify the interactions between colloidal particles. Then we characterized the nature of the interaction between the colloidal particles based on the analysis of the radial distribution function in the observed phases. **Figures 7** and **9** show the obtained $g(r)$ of the gas and liquid (low-density and high-density) phases, respectively. Every $g(r)$ exhibits the highest particle density at the distance of the first maxima (d_{NN}, the nearest-neighbor distance). For the case in **Fig. 7(a)**, d_{NN} is 4.5 μm and the particles are 1.5 μm apart. Because the interparticle gaps (= d_{NN} - 3 μm) decrease from 1.5 μm to 300 nm as the packing fraction increases (**Fig. 7(a)**, **Fig. 7(b)**, and **Fig. 9(a)**), the absence of direct contact between the particles suggests charge stabilized interactions.

The asymptotic behaviors of the total correlation functions $h(r) = g(r) - 1$ for the charge-charge correlation and the density-density correlation have been extensively studied. The change from a monotonic to an oscillatory decay under certain thermodynamic conditions can be understood by the Kirkwood cross-over and Fisher-Widom cross-over [40, 41]. Both decays are approximately described by the same relationship as

$$h(r) \approx \frac{e^{-\alpha_0 r}}{r}\cos\left(\alpha_1 r - \theta\right) \tag{5}$$

where α_0^{-1} is the exponential decay length, $2\pi/\alpha_1$ is the oscillatory wavelength, and θ is the phase. Because the liquid phase clearly exhibits oscillatory damping of $g(r)$, we examined the asymptotic behavior by plotting $\ln|rh(r)|$ as a function of r. **Figure 10** shows the behavior of $\ln|rh(r)|$ fitted by the two exponential decays with short- and long-range decay lengths. Although both decays indicated the same oscillatory wavelengths of 3.2 μm, the short- and long-range decay lengths were calculated as 3.2 μm (~σ_-) and 35 μm (>10σ_-), respectively. In the theory for the asymptotic behaviors of a screened Coulomb system, $g(r)$ can be represented by the short-range and

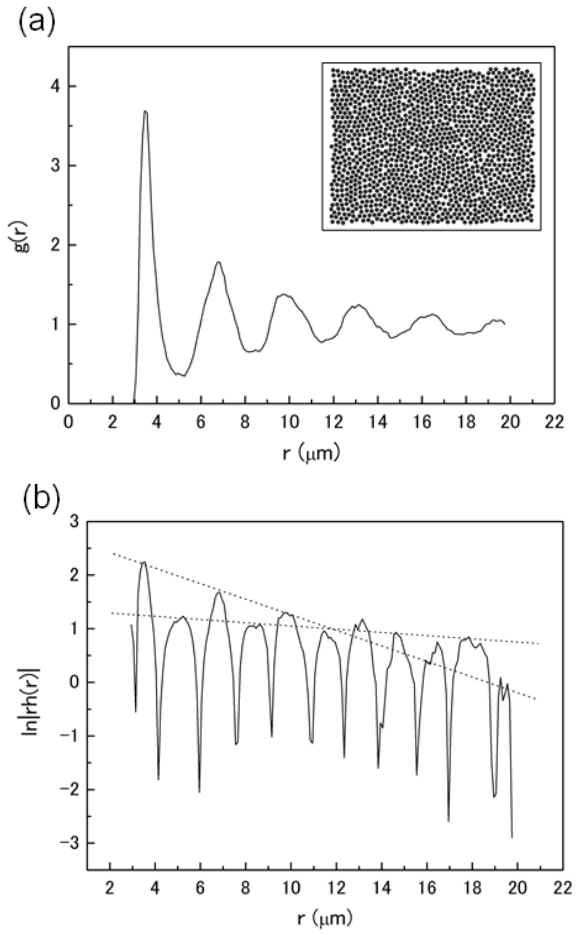

Fig. 10 Radial distribution function g(r) of the high-density liquid phase and oscillatory damping of the total correlation function h(r). (a) Inset shows the particle configuration of the liquid with a packing fraction of 0.32 and CN=6.0. (b) Natural logarithm of |rh(r)| as a function of distance r. Oscillatory damping of h(r) (dotted lines) indicates the short-range and long-range decay lengths, which are 3.2 μm and 35 μm, respectively.

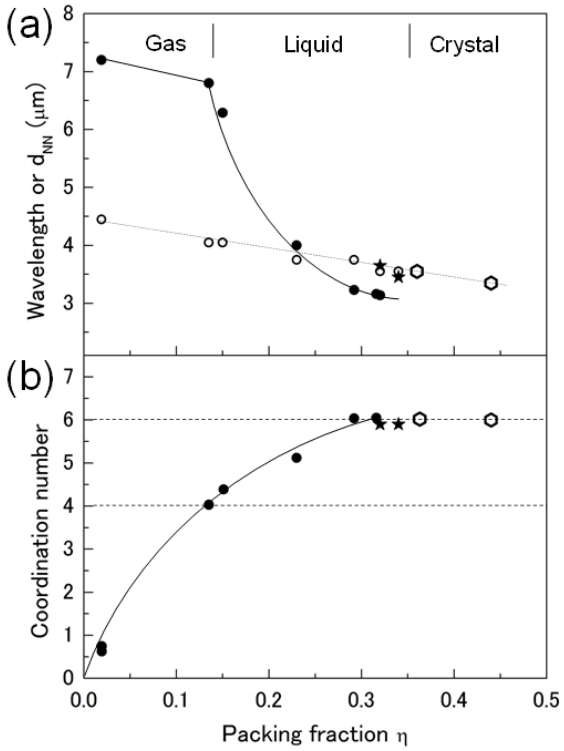

Fig. 11 Wavelength, nearest-neighbor distance dNN, and coordination number of the colloid particles as a function of packing fraction. (a) Filled circles with a solid line and filled stars indicate wavelengths for the long-range oscillations of |rh(r)|. Open circles and hexagons with dotted lines denote dNN obtained from the first maxima of g(r). Circles are data from the gas and liquid phases, hexagons indicate hexagonal crystals, and filled stars are data from the cross region of the high-density liquid line (solid line in Fig. 8). (b) Dependence of the coordination number on the packing fraction is compared to the wavelength and dNN using the same symbols. Dotted lines show coordination numbers of 4 and 6 where the gas-liquid and liquid-solid boundaries are observed.

the long-range correlation functions, which are related to the repulsive core interaction for an intermediate r and the Coulomb interaction for a large r [42]. Therefore, the short-range oscillatory damping is attributed to the density-density correlation due to core exclusion, whereas the long-range one is due to the charge-charge correlation caused by layering opposite charges. Additionally, a study on a one-component plasma system has shown that the oscillatory wavelengths for both mechanisms coincide in the asymptotic high-density limit [41]. Because a high-density liquid with a packing fraction of 0.32 coexisted with the hp crystal, which had a packing fraction of 0.36, possessing the same wavelength is reasonable.

Figures 11(a) and **(b)** plot the oscillatory wavelength with the long-range decay as a function of the packing fraction as well as d_{NN}, which works as a repulsive core, and the CN at each packing fraction, respectively. A wavelength of 7.2 μm is obtained in the gas phase at $\eta = 0.019$, but the value drastically decreases in the liquid phases with $\eta > 0.14$ and CN > 4. In the high-density region of the liquid phase, the wavelength drops below d_{NN}, and the CN almost reaches 6 near $\eta = 0.32$. Beyond η~0.3, hp crystals are found in the phase separation. Interestingly, the liquid phase in equilibrium with the solid phase has the smallest wavelengths, which are well below d_{NN} of the crystals.

These small wavelengths indicate that the fluctuation in the charge-charge correlation compacts the particles into a dense liquid state, and then core exclusion compels the particles into a crystalline order, that is, an order-disorder transition. The

charge-charge correlation works as a stabilization mechanism in the crystalline phase. The hp crystals are destabilized when the wavelengths are similar to the d_{NN} values (denoted by ★ in **Fig. 11(a)**). The liquid-solid transition can be explained according to the standard screening effect of salt ions [43]. Because the surface charge density of the colloids is calculated as 1×10^{-3}C/m^2 (0.1 μC/cm^2) at a 2×10^{-5} M salt concentration, mapping the values in the liquid-solid phase diagram of the Yukawa system supports a consistent phase behavior.

Recently, a field-theoretical description of ionic solutions has been successfully applied to the phase behaviors of ionic systems. Ciach et al. introduced a mesoscopic theory to systematically explain the phase diagrams of size- and charge-symmetric and asymmetric ionic systems [44, 45]. The coarse-graining (Landau-Ginzburg-Wilson) approach under the mean-field approximation enables the stability of ionic systems to be analyzed according to a linear combination of two order-parameters: the density of charge and the density of mass. The evaluation of the order parameters clarifies the importance of the charge-ordered phase in gas-liquid phase separation and its stability is represented by a spinodal line. The charge-ordered phase is realized by the arrangement of ions so that each charge is surrounded by neighboring charges with opposite signs due to the natural tendency of ionic solutions to be locally charge neutral [46]. At the spinodal line of the charge-charge correlation, this charge-ordering extends over a long distance to form a charge density wave (CDW). According to the extended theory of the Landau-Ginzburg-Wilson approach for the colloidal limit, a CDW is realized when $T^* \leq 1.54Z\_\eta$ is satisfied. The theoretical wavelength of the CDW in a very dilute gas phase is derived as $2.55\sigma\_$ and is independent of the packing fraction [44]. Using the experimentally obtained values for the effective charges and packing fractions, the large inequality of $0.4<<1.54\times10^4\times0.01=154$ is confirmed. The observed wavelengths in the gas phases remain nearly constant, and the values between 6.8–7.2 μm agree with the theoretical one of 7.65 μm. Furthermore, the decrease in the wavelength as the packing fraction increases qualitatively coincides with the results of the large asymmetrical electrolyte of 1:10^4 in charge and 1:10^3 in size [45]. Thus, the theoretical estimates are consistent with the experimental observation and the CDW is indicated to be an underlying mechanism which determines the phase stability of charged colloids.

4.3 Effects of the bottom substrate

The cell wall has several effects, such as an attractive pair interaction between like-charged particles and suspended colloidal particles accumulating near the wall [22-27]. Lobaskin et al. have realized a similar two-dimensional system using a laser confinement technique at high colloidal densities and low-salt conditions [24-26]. The extracted effective pair potentials using the inverse MC method show a long-range attractive component at $\rho\sigma^2 = 0.226$, which is not obtained at lower densities. In our experiments, $\rho\sigma^2$ is 0.32 at an initial particle concentration of 0.1 vol %, which exceeds the Lobaskin's value of 0.226. Because the attractive component increases with particle number, Lobaskin et al. claim that many-body interactions are the major origin. In this study, colloidal condensation occurred for particle densities less than 0.226 (see **Fig. 3** at 0.05 vol % and **Fig. 4** below 0.10 vol %). The detailed physics of many-body effects should be further investigated.

As studied by Grier and co-workers [22], the effective pair potential of like-charge colloids becomes negative (attractive) when the charged particles are located near the glass plates. Because the configuration reported here is quite similar to Grier's experiments, we need to discuss the contribution of the glass wall in gas-liquid-solid condensation. Grier et al. [22] report no evidence of an attractive potential when the bottom glass is coated with Au. To confirm the relevance to Grier's attractive potential, we replaced the bottom glass by the glass coated with a 20 nm Au film. However, we did not observe any differences in the phase appearance of colloidal condensation between glass and Au.

Ito et al. reported a concentration effect of polystyrene particles at the vicinity of glass interface [47, 48]. The particle concentration near the interface is 2.5 times higher than the bulk concentration when the concentration of added NaCl is nil, becomes smaller with increasing salt concentration, and disappeared when the NaCl concentration was 10^{-4} M. We initially designed to realize the mono-particle layer by adjusting the solvent density and the total particle numbers were set to a bottom area occupation of 25-50 % on the substrate. The occupation area is too small to affect the quantitative contribution to the radial distribution function of lateral condensates. We can quantitatively discuss the particle-particle interactions using the radial distribution function.

The macroscopic structure of phase separation shown in **Fig. 5** is unique. Previous reports do not mention this type of self-organized structure where the high-density crystalline phase is located at the center of the colloidal condensate, and the other phases appear as the density decreases toward the periphery. This type of structure is qualitatively explained by the juxtaposition of the potential field (JPF) [49-51]. The high-density crystalline region realizes a high electrostatic potential field due to the overlapping potentials of colloid ions, which cause the counterions to be inhomogeneously distributed within the crystalline structure. Additionally, the bottom boundary strengthens the JPF stabilization of colloidal condensation. Because counterions are confined to the mono-particle layer due to the charge neutrality requirement of highly charged colloids, only the layer space is permitted for diffusion. The higher concentration of the counterions inside the crystalline phases

induces diffusion of counterions toward the radial direction. Thus, less dense phases are formed according to the balance between the confining force of the colloidal particles and the diffusional forces of the colloids and counterions. However, as shown in **Fig. 5**, the crystalline region revealed the coalescence of crystals originated from nucleation and growth processes before the appearance of the equilibrium structure. This means that dynamic mechanisms also contribute the appearance of the large packing fraction gradient along the radial direction. To explain the colloidal self-organization from a microscopic level, a study by using MD simulations is in progress.

5. Conclusions

Herein we report a new system of colloidal phase separation where colloid ions are gravitationally confined near a glass wall and demonstrate the gas-liquid and liquid-solid phase diagrams. Because past experiments have separately examined colloidal gas-liquid and liquid-solid phase changes, the absence of a unified phase diagram has prevented mutually contradictory arguments in theories and experiments concerning the phase behaviors of charged colloids from being resolved. The obtained results show how the coexistence of spatial fluctuations in the charge-charge correlation and the density-density correlation between very large particle ions and small counterions determines the stability of various phases. We can conclude that our system is a promising model to test new theories and computer simulations concerning colloidal phase separation. Moreover, colloidal self-assembly on the substrate has important technical applications, e.g. it may produce photonic materials. Although gravitational sedimentation, which we adopted, is one of the most accepted processes to prepare new functional materials, it contains many unknown physical phenomena, such as hydrodynamic interactions between particles and the wall, electric field effects due to the presence of dielectric substances, and like-charged interactions between colloids. We believe the reported system offers new opportunities to investigate a wide range of interesting problems from modeling to processing.

Acknowledgments

The authors have benefited from discussions with Junpei Yamanaka, Kensaku Ito, and Ikuo Sogami. This research was partially supported by the Ministry of Education, Science, Sports and Culture, Grant-in-Aid for 4901, 20200004, 2008.

References

1) Y. Levin: Rep. Prog. Phys., **65** (2002) 1577.
2) L. Belloni and J. Phys: Condens. Matter, **12** (2000) R549.
3) U. J. Gasser and Phys: Condens. Matter, **21** (2009) 23101.
4) C. Vega, F. Bresme and J. L. F. Abascal: Phys. Rev., E **54** (1996) 2746.
5) C. Vega, J.L.F. Abascal, C. McBride and F. J. Bresme: J. Chem. Phys., **119** (2003) 964.
6) J.B. Caballero, A.M. Puertas, A. Fernández-Barbero and F.J.J. de las Nieves: J. Chem. Phys., **121** (2004) 2428.
7) J.B. Caballero, E.G. Noya and C.J. Vega: J. Chem. Phys., **127** (2007) 244910.
8) A.-P. Hynninen, M.E. Leunissen, A.van Blaaderen and M. Dijkstra: Phys. Rev. Lett., **96** (2006) 018303.
9) M.E. Leunissen, C.G. Christova, A.-P. Hynninen, C.P. Royal, A.I. Campbell, A. Imhof, M. Dijkstra, R. van Roij and A. van Blaaderen: Nature **437** (2005) 235.
10) A.-P. Hynninen and A.Z. Panagiotopoulos: Phys. Rev. Lett., **98** (2007) 198301.
11) A.-P. Hynninen and A.Z. Panagiotopoulos: Mol. Phys., **106** (2008) 2039.
12) A.-P. Hynninen and A.Z. Panagiotopoulos: J. Phys. Condens. Matter, **21** (2009) 465104.
13) S. Hachisu, Y. Kobayashi and A. Kose: J. Colloid Interf. Sci., **42** (1973) 342.
14) K. Takano and S. Hachisu: J. Chem. Phys. **67**, 2604 (1977).
15) S. Hachisu and Y. Kobayashi: J. Colloid Interf. Sci. **46**, 470 (1974).
16) N. Ise: Proc. Jpn. Acad. Ser., B **83** (2007) 192.
17) B.V.R. Tata and S.S. Jena: Solid State Comm: **139** (2006) 562.
18) H. Yoshida, N. Ise and T. Hashimoto: J. Chem. Phys., **103** (1995) 10146.
19) K. Ito, H. Yoshida and N. Ise: Science, **263** (1994) 66.
20) I. Sogami and N. Ise: J. Chem. Phys., **81** (1984) 6320.
21) A.K. Sood: Solid State Phys., **45** (1991) 1.
22) J.C. Crocker and D.G. Grier: Phys. Rev. Lett., **77** (1996) 1897; M. Polin, D.G. Grier and Y. Han: Phys. Rev., E **76** (2007) 041406.
23) J. Baumgartl and C. Bechinger: Europhys. Lett., **71** (2005) 487; A. Ramírez-Saito, C. Bechinger and J.L. Arauz-Lara: Phys. Rev., E **74** (2006) 030401.
24) M. Brunner, C. Bechinger, W. Strepp, V. Lobaskin and H. H. Von: Grünberg, Europhys. Lett., **58** (2002) 926.
25) R. Klein, H.H. von Grünberg, C. Bechinger, M. Brunner and V. Lobaskin: J. Phys. Condens. Matter, **14** (2002) 7631.
26) V. Lobaskin, M. Brunner, C. Bechinger and H.H. von Grünberg: J. Phys. Condens. Matter, **16** (2003) 6693.
27) H.H. von Grünberg and E.C. Mbamala: J. Phys., Condens. Matter, **13** (2001) 4801.
28) R.E. Beckham and M.A. Bevan: J. Chem. Phys., **127** (2007) 164708.
29) W.B. Russel, D.A. Saville and W.R. Schowalter: Colloidal dispersions, Cambridge University Press, Cambridge, U.K. (1989).
30) R.W.O'Brien and R. J. Hunter: Can. J. Chem,. **59** (1981)1878.
31) R.W. O'Brien and L.R. White: J. Chem. Soc. Faraday II, **74** (1978) 1607.
32) R. Hunter: Zeta Potential in Colloid Science, Principles and Applications, Academic Press, New York, 1981.
33) M. Ishikawa and R. Kitano: Langmuir, **26** (2010) 2438.
34) S. Mori and H. Okamoto: Fusen, **27** (1980) 117.
35) http://rsb.info.nih.gov/ij/index.html.
36) D.A. McQuarrie, Statistical Mechanics, University Science Books, California, 2000.
37) S. Alexander, P.M. Chaikin, P. Grant, G.J. Morales and P. Pincus: J. Chem. Phys., **80** (1984) 5776.
38) E. Trizac, L. Bocquet and M. Aubouy: Phys. Rev. Lett., **89** (2002) 248301.

39) L. Bocquet, E. Trizac and M. Aubouy: J. Chem. Phys., **117** (2002) 8138.
40) R.J.F. Leote de Carvalho and R. Evans: Mol. Phys., **83** (1994) 619.
41) R.J.F. Leote de Carvalho, R. Evans and Y. Rosenfeld: Phys. Rev. , E **59** (1999) 1435.
42) G. Stell: in New Approaches to Problems in Liquid State Theory, edited by C. Caccamo, J.-P. Hansen and G. Stell, Kluwer Academic, Dordrecht, 1999, pp. 71-89.
43) A. Toyotama, T. Sawada, J. Yamanaka and K. Kitamura: Langmuir, **19** (2003) 3236.
44) A. Ciach, W.T. Gozdz and G. Stell: J. Phys, Condens. Matter, **18** (2006) 1629.
45) A. Ciach, W.T. Gozdz and G. Stell: Phys. Rev., E **75** (2007) 051505.
46) P. Keblinski, J. Eggebrecht, D. Wolf and S. R. Phillpot, J. Chem. Phys., **113** (2000) 282.
47) K. Ito, T. Muramoto and H. Kitano: J. Am. Chem.,Soc., **117** (1995) 5005.
48) T. Muramoto, K. Ito and H. Kitano: J. Am. Chem. Soc., **119** (1997) 3592.
49) K S. Schmitz: Langmuir **13** (1997) 5849.
50) K.S. Schmitz: Phys. Chem. Chem. Phys., **1** (1999) 2109.
51) K.S. Schmitz: Langmuir **15** (1999) 4093.